1D/2D Hybrid Te/Graphene and Te/MoS$_2$: Multifaceted Broadband Photonics and Green-Energy Applications

Tuhin Kumar Maji, Kumar Vaibhav, Anna Delin, Olle Eriksson,* and Debjani Karmakar*

Cite This: ACS Appl. Mater. Interfaces 2022, 14, 51449−51458   Read Online
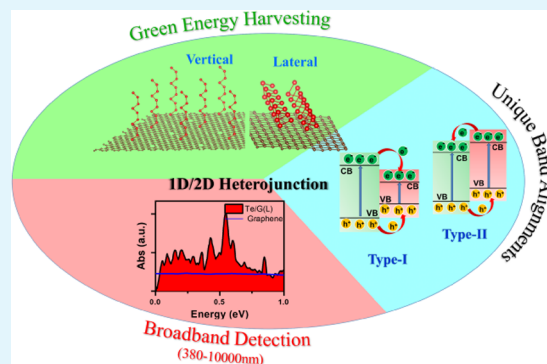
ACCESS | 📊 Metrics & More | 📖 Article Recommendations | 🗐 Supporting Information

ABSTRACT: We highlight the enhanced electronic and optical function-alization in the hybrid heterojunction of one-dimensional (1D) tellurene with a two-dimensional (2D) monolayer of graphene and MoS$_2$ in both lateral and vertical geometries. The structural configurations of these assemblies are optimized with a comparative analysis of the energetics for different positional placements of the 1D system with respect to the hexagonal 2D substrate. The 1D/2D coupling of the electronic structure in this unique assembly enables the realization of the three different types of heterojunctions, viz. type I, type II, and Z-scheme. The interaction with 1D tellurene enables the opening of a band gap of the order of hundreds of meV in 2D graphene for both lateral and vertical geometries. With both static and time-dependent first-principles analysis, we indicate their potential applications in broadband photodetection and absorption, covering a wide range of visible to infrared (near-IR to mid-IR) spectrum from 380 to 10 000 nm. We indicate that this 1D/2D assembly also has bright prospects in green-energy harvesting.

KEYWORDS: IR detection, 1D/2D heterojunction, TDDFT, energy harvesting, tellurium nanorod

INTRODUCTION

The genesis of van der Waal heterojunctions with systems of different dimensionalities offers a possibility of flexible atomic-scale integration of materials with widely distinct electronic properties and thus widens the horizon of diverse photonics and green-energy applications.[1−3] Befitting these attributes, one-dimensional (1D)/two-dimensional (2D) hybrids offer the advantages of integrating the leverages of 1D nanostructures such as better electron transport, higher aspect ratio, and larger specific surface area for improved absorption of light with the endowed plus-points of 2D materials such as larger concentration of active sites, shorter diffusion length, and high mobility. Thus, such systems expedite a faster transfer of free charge, facilitating the separation and migration of photo-generated carriers.[4−8] The recent surge of multifarious applications of hybrid materials in the fields of photodetection and energy harvesting comprises both the lateral and vertical stacking geometries, synthesized by ex and in situ modes.[9−12] Among the numerous reported 1D/2D hybrids, one should mention significant applications like the enhanced photo-detectivity of Te-nanorod/graphene in the infrared (IR) range,[1] broadband photodetection of Se/InSe,[13] improved optoelectronic activity of 1D double perovskite/2D materi-als,[14] utilization of WO$_{3−x}$/graphene as a pressure sensor,[15] carbon nanotube/graphene or MoS$_2$ as a thermal sensor,[16] Bi$_2$S$_3$/MoS$_2$ as a photodetector and rectifier,[17,18] TiO$_2$/Bi$_2$WO$_6$ as a gas sensor,[19] and C$_3$N$_4$/graphene as an improved

anode material for Li-ion batteries.[20,21] Moreover, 1D/2D hybrids are also well known to have widespread applications in the field of green and sustainable energy harvesting by providing better pathways for the separation and migration of charge carriers for systems like TiO$_2$/ZnIn$_2$S$_4$,[22] CdS/ZnIn$_2$S$_4$,[23] CdS/MoS$_2$,[11] TiS/Mxene,[24] FeSe$_2$/MoSe$_2$,[25] car-bon nanotube/phosphorene,[26] and many more.[4,27−29]

The photoactive performances of semiconducting photo-detectors highly depend on the optimized regime of the wavelength detection, specific to a particular combination of the hybrids. While there are numerous systems like silicon, InGaAs, or GaN having utilizations in the ultraviolet (UV) and visible (Vis) range, materials encompassing the full infrared (IR) range are less frequent. IR detectors are separately categorized as photonic and thermal detectors with activities in the near (NIR) plus mid (MIR) and far-IR (FIR) ranges, respectively.[30,31] The faster performance and compact sizes of the photonic IR detectors have stimulated the search for effective materials possessing optical activities in the full IR range. Suitable materials may replace the costly and
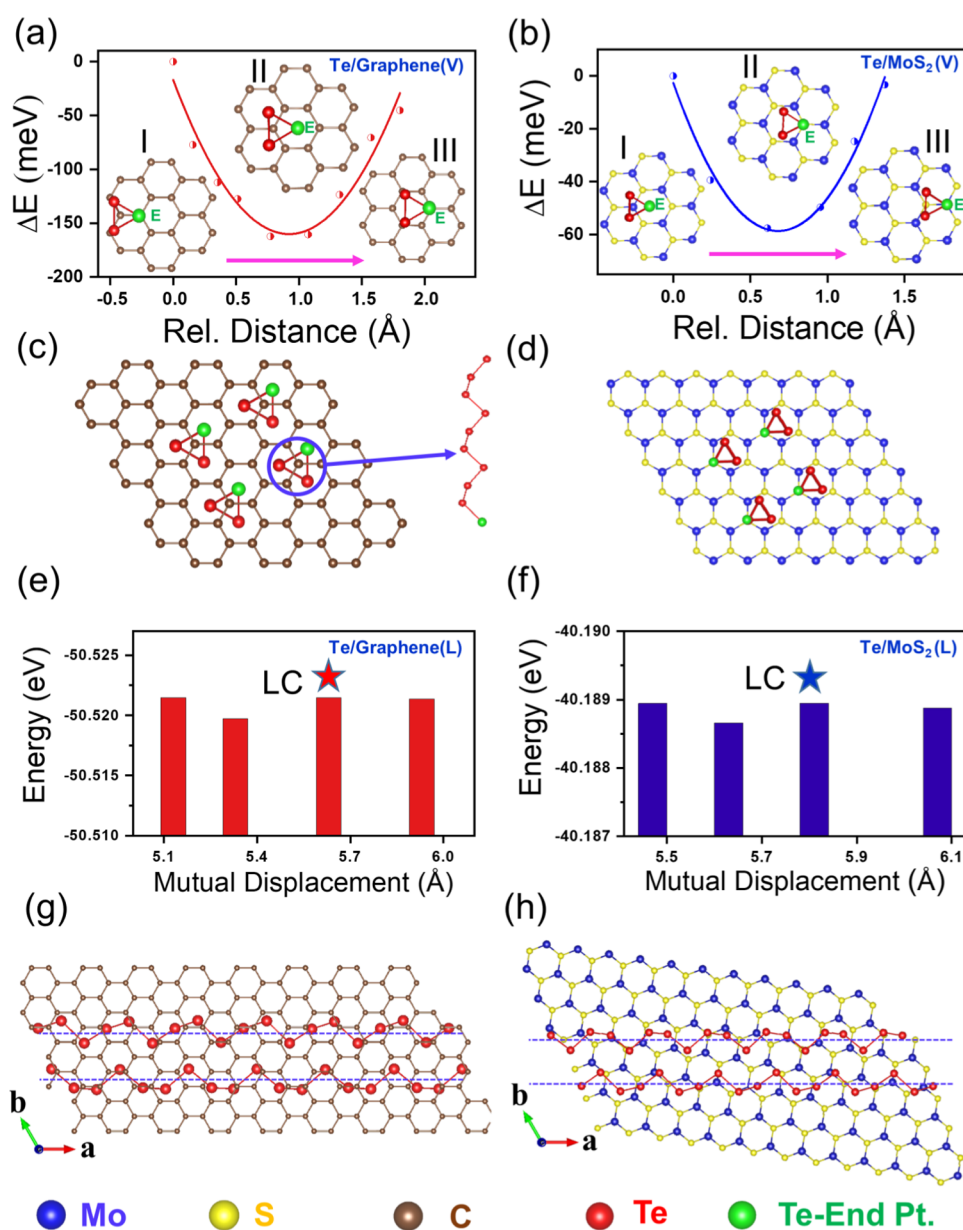
Figure 1. Ground-state energies (with respect to a fixed vertex point) and corresponding structural images of (a) Te/graphene(V) and (b) Te/MoS$_2$(V) heterojunctions. The lowest-energy structure of (c) Te/graphene(V) and (d) Te/MoS$_2$(V). For lateral heterojunctions, ground-state energies with respect to a fixed line, parallel to the NR axes and passing through the center of the ML of (e) Te/graphene(L) and (f) Te/MoS$_2$. The ground-state energy has been plotted after normalizing with the number of Te-atoms. The lateral configurations (LC) used for further calculation are indicated on each graph. The corresponding structural images are presented in (g) Te/graphene(L) and (h) Te/MoS$_2$(L).

complicated synthesis of commonly used semiconductor alloy materials like HgCdTe or semiconductors like Pb chalcogenides or InSb[32−36] with simple chemical synthesis.

After the advent of novel 2D materials like graphene or transition metal dichalcogenides (TMDC), broadband photodetection has gained a new pace.[37,38] Graphene is well known for its property of ultra-broadband detection as a result of its zero-band-gap nature.[39] However, because of the short lifetime of the hot carriers as a result of their ultrafast recombination and the resulting limited responsivity of metal-contacted bare graphene detectors and p−n junctions,[40−43] there are continuous efforts to enhance the performance upon coupling with microcavities,[44,45] plasmonic structures,[46,47] quantum dots,[48] or fabricating stacked structures with TMDC[49,50] and thus increasing the lifetime of the carriers through physical

separation. TMDC systems like MoS$_2$ in its monolayer form have displayed optical activity in the visible range.[51,52] A multitude of efforts have been dedicated to obtaining broadband photodetection from monolayer or multilayered MoS$_2$ after combining them with plasmonic nanostructures[50] or other TMDC systems.[51] α-Te, on the other hand, is a direct-band-gap semiconductor, having excellent optical activity in the FIR range.[53−55] Moreover, it is a well-known 1D van der Waals material, consisting of an $a−b$ plane van der Waals stacked array of c-axis-oriented single helices of Te[55] and thus can be transformed into an extremely thin 1D helix by using standard liquid-crystal exfoliation techniques. Prior experimental studies by Pradhan et al. had demonstrated a remarkably high photoresponse of the graphene/Te nanorod assembly in the NIR range,[1] which is far higher than the

photoresponse of conventional NIR detectors. Therefore, the hybrid of 1D Te with standard 2D materials like graphene or MoS_2 may provide a suitable playground to intricately explore the stacking and interaction of 1D/2D hybrids.

In this work, we indicate the remarkable application potential of the heterojunction of the 1D single helix of tellurene, the building block of Te-nanorod (Te-NR), with the 2D monolayer of graphene or MoS_2 in lateral and vertical stacking geometries and comprehensively analyze their electronic structure and optical responses. Four different types of 1D/2D heterojunctions are explored, viz., (1) Te-NR on graphene in lateral (Te/graphene(L)) and (2) in vertical geometry (Te/graphene(V)), (3) Te-NR on MoS_2 in lateral (Te/MoS_2(L)), and (4) in vertical geometry (Te/MoS_2(V)).

Computational Methodology. To study the electronic properties of the Te/M interface or Te/G interface, we have initially constructed interfaces by joining the two lattices by the coincidence site lattice (CSL) method, as implemented in the Atomistic Toolkit 15.1 package.[56] A $8 \times 4 \times 1$ graphene or MoS_2 layer has been taken as the base 2D structure and Te rods are stacked vertically or horizontally on the top of it. In all of the cases the strain has been minimized.

For the static density functional calculation, we have used spin-polarized plane-wave pseudopotential methods with projector augmented wave (PAW) formalisms as implemented in the Vienna Ab initio Simulation Package (VASP).[57,58] The ionic positions of the individual interfaces are relaxed to obtain the ground-state energy configuration. A vacuum of ~10 Å is introduced at the top and bottom of the interface to avoid periodic replication of the system. The exchange−correlation interactions are treated with the generalized gradient approximation (GGA) with Perdew−Burke−Ernzerhof (PBE) functionals.[59] Interface-induced van der Waals interactions are taken care of after including a semiempirical dispersion potential to the density functional theory (DFT) energy functional according to the Grimme DFT-D2 method.[60] The cutoff energy for the plane-wave expansion is set as 500 eV and a Monkhorst−Pack grid of $5 \times 5 \times 3$ is used for Brillouin zone sampling for all calculations. The ionic positions and the lattice parameters are relaxed by using the conjugate gradient algorithm until the Hellmann−Feynman force on each ion is less than 0.01 eV.

The static optical properties are calculated after using the Atomistic Toolkit 15.1 package,[56] with the GGA-PBE variant of exchange−correlation.

The time-dependent optical and magneto-optical properties are calculated with the all-electron full-potential linearized augmented plane-wave approach including local orbitals (FP-LAPW + lo) as implemented in the ELK7.4 code. The exchange−correlation potentials are calculated with local density approximation (LDA) using the Perdew−Wang/ Ceperley Alder functional. The interstitial plane-wave vector cutoff K_{max} is chosen such that $R_{mt}K_{max}$ is greater than or equal to 7 for all of the calculations, with R_{mt} being the smallest of all atomic sphere radii. The convergence criteria for total energy and RMS change in Kohn−Sham potential are kept as 0.0001 and 0.000001 eV, respectively. The valence wave functions inside the spheres are expanded upto $l_{max} = 10$ and the charge density was Fourier expanded upto $G_{max} = 12$.

Construction of the Heterostructure. α-Te is an extremely narrow-band-gap semiconductor in its bulk form having a band gap of ~0.35 eV in the FIR range,[53−55] as shown in Figure S1a. The bulk structure of α-tellurene consists of a van der Waal-bonded interpenetrating $a−b$ plane hexagonal array of c-axis-oriented covalently bonded single helix of Te,[55] as seen in Figure S1 of the Supporting Information (SI). An isolated infinite single helix is the building block of bulk Te and it possesses a band gap of ~1.2 eV (Figure S1). While graphene is a well-established zero-band-gap system, the monolayer (ML) of MoS_2 with a band gap of ~1.8 eV is at the boundary of NIR and Vis wavelengths (Figure S1). The 1D/2D heterojunction in the vertical stacking geometry is constructed from the truncated Te-NR with a sufficiently large average aspect ratio of ~15 and the $8 \times 4 \times 1$ supercell of the ML of graphene and MoS_2, with an appropriate vacuum slab. The process of energy optimization corresponding to the construction of the heterojunctions is summarized in Figure 1, where the ground-state energies for different configurations are compared and plotted. The steps of construction of both vertical and lateral heterostructures are described in the schematics, as presented in Figures S2 and S3 of SI. The configurations corresponding to the vertical placement of NR are ascertained in four steps. (I) The energetics corresponding to the placement of a single Te-NR is first assessed with respect to the graphene and MoS_2 hexagons. Figure 1a,b presents a comparison of the total energies of the Te/ graphene(V) and Te/MoS_2(V) heterojunctions for the vertical placement of the Te-NR with respect to a single hexagon. The pink arrow at the bottom indicates the relative direction of the displacement of the Te-NR, starting from one vertex of the hexagon to the diametrically opposite one. The top view of the NR is a red equilateral triangle and its end point is marked in green as E. The next two steps (II and III) are performed to reduce the mutual strain between the 1D and 2D systems. The integration of these two systems was carried out using the coincidence site lattice (CSL) technique, as implemented in the Atomistic Toolkit 15.1 package. The details of the CSL method are discussed in prior studies.[50,61] (II) The mutual strain between the surface cells of Te and the 2D systems is minimized by forming an appropriately large surface grid from both systems and forming a large-area heterostructure with them. (III) The mutual strain is further minimized by rotating the 2D layer about the stacking axis (c-axis) and calculating the mutual strain with variation of angles. Thus, the minimal strain configuration is determined with an optimal rotation of the 2D layer. This process is described in Figure S9 of SI. (IV) An assembly of four NRs, having the same lattice constants and inter-NR distances as the bulk system, are quantum confined to avoid the electronic overlap of the periodic images from the consecutive cells. The assembly of these four NRs resembles a realistic 1D nanostructure of Te, having close resemblance with the experiment. This full process of formation of the heterojunction is described in Figure S2.

The analysis of placement of 1D NR with respect to a single hexagon reveals that the optimized position of the NR is at the center and at the S-vertex of the hexagons for graphene and MoS_2, respectively. For higher densities of Te-NRs, Figure 1c,d presents the top view of the energetically optimized vertical array of Te NR on the graphene and MoS_2 monolayer. The effects of truncation-induced quantum confinement and formation of an assembly of four NRs on the band structures of Te are evident from Figure S4 of SI, where we compared the evolution of band gaps of (a) one infinite NR with those of a (b) truncated NR and (c) the assembly of four NRs. For the vertical heterojunction, the interfacial strain between the

surfaces is minimized to <5% and the other parameters of strain minimization are described in Table S3 of SI.

The lateral heterojunctions are constructed with the same 2D layers and with infinite NRs. The schematic for the construction is depicted in Figure S3 of SI. For lateral heterojunctions, we have worked with single-helix structures of Te, as placement of realistic NRs with multiple helices may lead to a complicated structural distortion masking the electronic effects. Figure 1e,f compares the total ground-state energies of the heterojunction normalized by the number of Te-atoms with respect to different configurations, as presented schematically in Figure S3. In these configurations, the axial displacements of the two laterally placed Te-NRs along the *a*-axis are varied with respect to a line (green in color in Figure S3) parallel to the *a*-axis and passing through the center of the ML. For different lateral configurations, the ground-state energies are quite comparable with respect to the variation of their relative displacements. This indicates that the probability to generate multiple lateral configurations with the variation of thermal energies is quite high. For two such NRs, the lateral heterostructures are optimized as in Figure 1g,h, corresponding to the configuration LC, as marked in Figure 1e,f, after avoiding the electronic cross-talking from their periodic replication. However, for lateral placement of NRs, there is no deterministic minimum energy configuration. Band dispersion of the double-NR assembly is presented in Figure S4d, which is similar to the infinite NR band structure (Figure S4a), except for a little modification of the band gap.

The formation energies of the hybrid systems are calculated using the relation $E_{form} = E_{1D/2D} - E_{1D} - E_{2D}$ and the formation energies per Te atom for the lateral and vertical heterostructures are presented in Table S2 of the SI. However, there can be no comparison of the formation energies of these two heterojunctions as the vertical assembly is constructed from finite NRs and the lateral ones are constituted of infinite NRs. In practical experimental situations, the vertical growth of Te-NR may involve an epitaxial high-temperature process,[62,63] whereas the synthesis of the lateral heterojunctions can be materialized by mechanical processes like drop-casting or spin-coating of the 2D layers.[1] The experimental results and the semiconducting nature of the system are highly dependent on the density of NRs on the 2D systems. Very high densities of 1D systems on 2D layers may lead to an altogether metallic nature of the band structures, as can be seen in Figure S11 of SI, where a high concentration of 1D structures was deliberately chosen to see its impact on the band structures.

Our aforementioned constructed heterojunctions resemble logically the practical systems. The experimental lateral heterojunction may have a longer length of Te NRs, as the systems are mostly prepared by drop-casting the Te NRs. The vertical heterojunctions will need high-temperature epitaxial growth, where the length of the Te NRs is bound to get limited.

■ RESULTS AND DISCUSSION

Electronic Structure and Band Alignment. After the accomplishment of geometrically optimized 1D/2D structures, we proceed to investigate the electronic structures of all four possible heterojunctions. For the lateral heterojunction, the electronic structure is affected by (a) structural distortion and (b) interlayer charge redistribution due to finite hopping interactions across the interface. In addition to these two effects, for the vertical heterojunction, there are additional

impacts from the truncation of the NRs. To analyze the individual impacts of these three effects, we investigated the band structures of the individual components of all four structurally optimized heterojunctions after decoupling the 2D and 1D components, and the results are plotted in Figures S5−S8 in SI, where we have taken all of the four structurally relaxed heterojunctions and considered three systems, viz. (a) Te NR 1D assembly after removing the 2D structure, (b) only 2D structure after removing the 1D assembly, and (c) the combined structure. In general, the structurally relaxed and distorted $8 \times 4 \times 1$ supercell of graphene is metallic with narrow-band crossings of linearly dispersed graphene $2p_z$ bands (Figures S5b and S6b) near the Γ-point. There is also a shift of the Dirac band crossings from the *K* to Γ-point. This is due to the fact that for the Brillouin zone (BZ) of the $8 \times 4 \times 1$ supercell, the *K*-point of the hexagonal unit cell of graphene is folded to the Γ-point.[64,65] We have elaborated this aspect in SI (Figure S1e,f). The corresponding BZs of the unit cell of graphene and the $8 \times 4 \times 1$ supercell of graphene are depicted in Figure S5e,f of SI, respectively. Additionally, due to the distortion-induced lowering of symmetry, there is an increment in the total number of bands. The monolayer of MoS_2, being a trilayer, has retained its direct-band-gap nature at the *K*-point. The interlayer charge redistribution and modification of van der Waals interactions due to the presence of the 1D system do not induce significant shift of the band edges of MoS_2 (Figures S7b and S8b).

Te/Graphene(L) Heterojunction. In zeroth-order approximation, the assembly of two infinite NRs is semiconducting with a band gap of ∼1.1 eV and the distorted graphene layer beneath it is metallic. In a lateral heterojunction, the Fermi level (E_F) of graphene is energetically situated below the valence band of the double Te-NR assembly (Figure S4d), promoting a finite probability of hopping of carriers from the valence band of Te to the metallic graphene. In the combined structure, electrons with higher effective masses are transferred from the highly localized Te 5p bands (red) to the linearly dispersed graphene $2p_z$ (green) levels, having carriers with lower effective mass, leading to an n-type doping. The interfacial charge redistribution and hybridization with Te 5p flat bands push the partially unoccupied graphene $2p_z$ levels to below the E_F. These hybridized occupied levels with heavier electrons interact with the lighter electrons in the partially occupied $2p_z$ levels of graphene at a very narrow range of energies near the Γ-point and thus pushes the occupied part of the band above E_F. This whole process, inciting the opening of a direct band gap of ∼130 meV at the Γ-point of graphene, is presented in a schematic in the lower panel of Figure S4. At each crossing with flat Te 5p bands, due to the finite hopping and electronic interaction between carriers with different effective masses, the $2p_z$ bands of graphene are gapped, as can be seen from the layer-projected band structure of graphene in Figure 2a. The presence of Te NR acts like a first-order perturbation to open a small band gap in graphene $2p_z$ levels due to electronic interactions, keeping almost the same carrier mobility in graphene. Hence, after the formation of the heterojunction, the band gap of graphene is within the band gap of Te-NR and thus, it resembles a type-I heterojunction. The schematic of the band alignment, indicating the illumination-induced interlayer carrier flow from Te NR to graphene and reverse, is presented in Figure 2b. Bader analysis conveys that for each Te atom, ∼1.2*e* is transferred from Te to graphene, as seen in Table 1. These transferred charges are
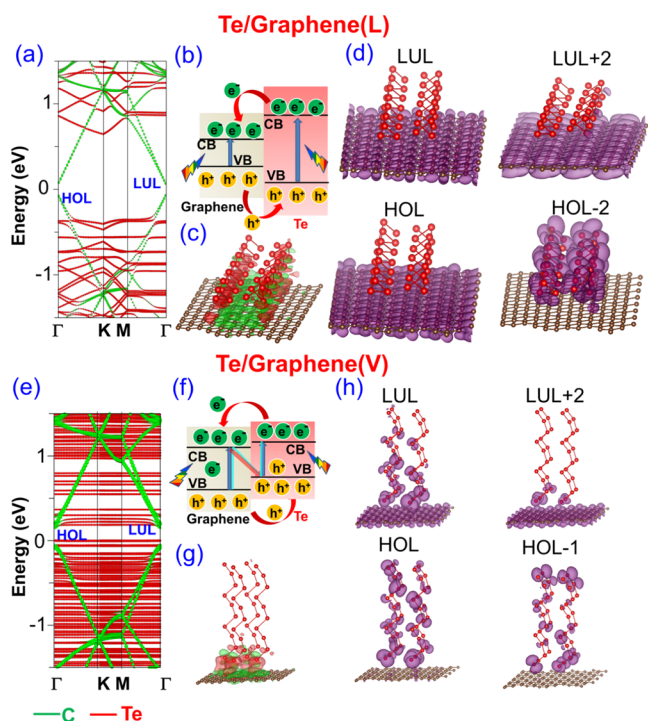
Figure 2. (a) Band structure and (b) corresponding type-I band alignment of Te/Graphene(L), (c) charge density difference, and (d) band projected charge density of Te/Graphene(L). (e) Band structure and (f) corresponding type-II and Z-scheme band alignment of Te/Graphene(V), (g) charge density difference, and (h) band projected charge density of Te/Graphene(V). The fatbands of graphene and Te are colored as green and red, respectively. HOL and LUL represent the highest occupied level and lowest unoccupied level.

Table 1. Bader Charge Analysis and Fermi Energy Table of the Different Heterojunctions

system		Te/graphene(V)	Te/graphene(L)	Te/MoS$_2$(V)	Te/MoS$_2$(L)
Bader charge (per atom)	Te	−1.64	−1.25	−1.11	−0.78
	G	0.006	−0.017	-	-
	MoS$_2$	-	-	0.86	0.17

mostly located at the interface, as is evident from the charge density difference (CDD), calculated as $\rho_{CDD} = \rho_{1D/2D} - \rho_{1D} - \rho_{2D}$, with ρ being the charge density and plotted in Figure 2c. The experimentally observed photo-gating effects,[1] as can be explained from Figure 2b, is due to the photo-generated transfer of similar types of carriers and the resulting repulsion after a certain amount of accumulation, leading to an illumination-induced control of the band gap. The level-projected charge densities for the highest occupied level (HOL), lowest unoccupied level (LUL), and their adjacent significant levels (±2) taking part in the optical interactions are plotted in Figure 2d. Whereas the localized charges on Te-NR near the CB edge are transferred to the steep and hybridized levels of graphene, the lowest occupied levels are having contributions from both graphene and Te. The magnitude of the band gap indicates the potential use of this heterojunction as a broadband detector in the NIR to MIR range (2500−10000 nm).

Te/Graphene(V) Heterojunction. For the vertically stacked heterojunction, the decoupled contributions of the structural

distortion and the charge redistributions are depicted in Figure S6. The truncation-induced quantum confinement of Te NR assembly leads to highly localized levels in the molecular limit (Figure S6a) and graphene is metallic with narrow $2p_z$ band crossings near the Γ-point (Figure S6b). Lack of any covalent bonding with the C-atoms of graphene leads to an almost unchanged band gap in Te with very few mid-gap levels. The formation of the heterojunction leads to a charge transfer from Te 5p to graphene $2p_z$ and increases the number of mid-gap states in Te. Similarly, as in the case of the lateral heterojunction, the first-order perturbative effects of charge redistribution and interactions between different massive carriers open a direct band gap of ∼150 meV at the Γ-point of graphene (Figure S6c). For this heterojunction, interaction of Te with graphene is less prominent, leading to almost unhybridized Te levels, except at the Γ-point, as seen from Figure 2e. The E_F of the combined system shifts toward the conduction band, implying an initiation of n-type doping during the formation of the heterojunction. Bader analysis conveys a charge transfer of ∼1.6e per atom of Te-NR (Table 1). The corresponding zeroth-order band alignment, as in Figure 2f, may be represented as a combination of the Z-scheme and type-II heterojunction. Whereas its staggered nature will have a carrier flow typical to type-II heterojunction (red arrow), the proximity of the valence band maxima (VBM) of Te-NR and the conduction band minima (CBM) of graphene within a few hundreds of meV promotes a finite probability of photogenerated carrier hopping from the VB of Te-NR to the CB of graphene and vice versa. Albeit an effective charge separation, the lifetime of the carriers will be determined by two competitive mechanisms, viz. the charge separation due to the staggered type-II band-gap alignment (red arrows) and the recombination rate due to the Z-scheme band alignment (cyan arrows). The CDD and the level-projected charge densities, as presented in Figure 2g,h, convey that the highest occupied and adjacent levels are contributed by Te-NR, whereas the lowest unoccupied levels have contributions from both graphene and Te-NR, in corroboration with its band structure. The system may have a potential application in NIR-MIR broadband detection (2500−10 000 nm) as well as in photocatalytic energy harvesting.

Te/MoS$_2$(L) Heterojunction. The decoupled band structures of this heterojunction are presented in Figure S7, where the infinite NR assembly has a dispersed band structure (Figure S7a), with a band gap of ∼1 eV and MoS$_2$ with the same band gap (Figure S7b). The combined band structure, as presented in Figure 3a, clearly demonstrates a type-II heterojunction, having a staggered band alignment as presented in Figure 3b, where the VBM and CBM of the heterojunction are constituted of Te-NR and MoS$_2$, respectively, resulting an indirect band gap in the NIR range ∼1.23 eV. The band gaps of this order are quite conducive to the photocatalytic energy harvesting. The CDD, as presented in Figure 3c, indicates the additional charge in the heterojunction to be mostly located at the interface. The lowest and the highest occupied levels and their adjacent level-projected charge densities, as presented in Figure 3d, indicate the contributions by MoS$_2$ and Te-NR levels. During formation, there is a charge transfer of ∼1.1e per atom of Te to the MoS$_2$, according to Table 1 of Bader analysis, implying n-type doping. A type-II heterojunction is the most interesting one among all of the plausible types of heterojunction, having the potential for both broadband detection and energy-harvesting applications.[66] The band-
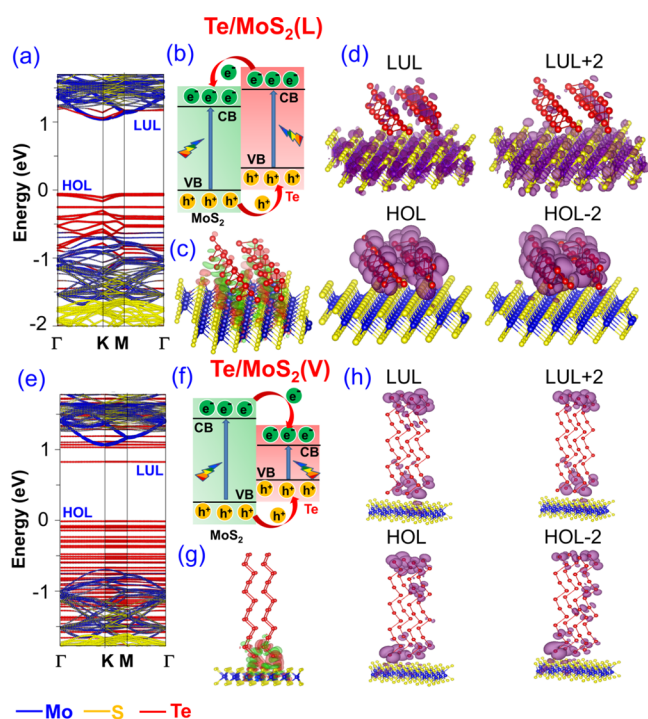
Figure 3. (a) Band structure and (b) corresponding type-II band alignment of Te/MoS$_2$(L), (c) charge density difference and (d) band projected charge density of Te/MoS$_2$(L). (e) Band structure and (f) corresponding type-I band alignment of Te/MoS$_2$(V), (g) charge density difference and (h) band projected charge density of Te/MoS$_2$(V). The fatbands of Mo, S, and Te are colored as blue, yellow, and red, respectively. HOL and LUL represent the highest occupied level and lowest unoccupied level.

lifetime.[67,68] The photogenerated electron−hole pairs are located in the two different layers, where the conduction electrons of Te-NR are transferred to the CB of MoS$_2$ and the holes at the VB of MoS$_2$ are transferred to the VB of Te-NR. In this manner, the separation and migration of the carriers may insinuate a longer lifetime for them, leading to a lesser rate of nonradiative recombination. Thus, this heterojunction has the possibility of a better performance in solar energy harvesting.

Te/MoS$_2$(V) Heterojunction. For the vertical heterojunction, the decoupled band structure in Figure S8 shows a modulated band gap of Te-assembly with a multitude of mid-gap levels (Figure S8a) due to the bonding of Te with S and unchanged MoS$_2$ bands (Figure S8b). In the zeroth-order approximation, the Te-band gap is clearly within the band gap of MoS$_2$, leading to a type-I band alignment. The level-projected band structure of this heterojunction is presented in Figure 3e, where the quantum confinement of Te-NR produces unhybridized localized levels and significantly reduces the mid-gap levels. There is a per atom charge transfer from Te-NR to the MoS$_2$ of ∼0.8e, expediting the n-type doping. The corresponding band-alignment diagram of the combined heterojunction, as depicted in Figure 3f, indicates that both the VBM and CBM of the combined system are contributed from the Te-NR and the holes and the electrons from the VB and CB of MoS$_2$ will populate the VB and CB of Te-NR. Whereas the CDD is mostly confined near the interface, as seen from Figure 3g, the level-projected charge densities for the highest occupied, lowest unoccupied, and their adjacent levels are entirely contributed by Te-NR, at par with its band structure. In this heterojunction, the localized Te levels at the mid-gap may act as trap states to the photogenerated electrons and thus may render a longer lifetime of the excitons.[67,68] The heterojunction has a direct band gap of 0.83 eV and can again be used as a broadband photodetector in the NIR range.

Optical Properties of the Heterojunctions. The potential of optical application of these four heterojunctions, as obtained from the combined electronic structure, can be
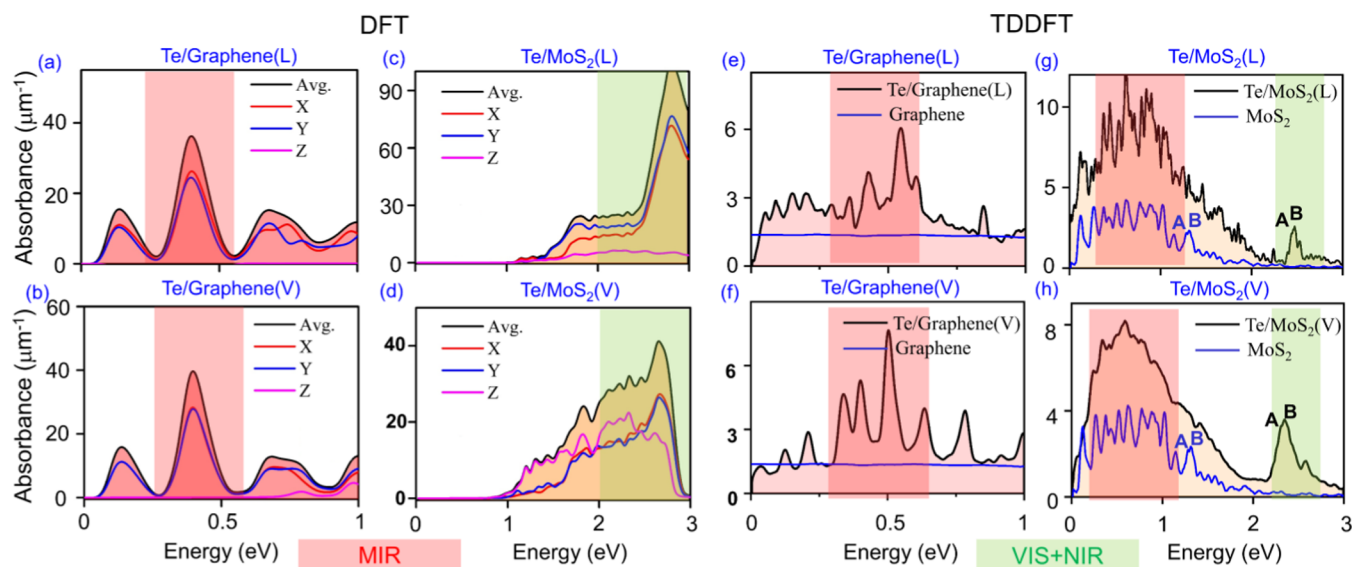
alignment diagram in Figure 3c distinctly indicates the potential of the present heterojunction in energy harvesting in the NIR and Vis range. In addition, it promotes the possibility of the formation of interlayer excitons with a longer

Figure 4. Static absorbances (from DFT) per unit optical length are plotted for (a) Te/Graphene(L), (b) Te/Graphene(V), (c) Te/MoS$_2$(L), and (d) Te/MoS$_2$(V) with their corresponding range of optical activity as shown in the lower panel. The time-dependent density functional theory (TDDFT) absorbance per unit optical length is plotted for (e) Te/Graphene(L), (f) Te/Graphene(V), (g) Te/MoS$_2$(L), and (h) Te/MoS$_2$(V) with their corresponding range of optical activity as shown in the lower panel.

further extended toward the calculation of their optical absorbance. The details of the calculation of the optical response are outlined in SI. Figure 4a−d presents the static optical absorbance per unit optical path for these four heterojunctions, as calculated from the density functional theory (DFT) by using the real (ε_1) and imaginary (ε_2) parts of the dielectric response as related by the Kramer−Kronig relation, the implications of which can be summarized as follows. First, the peaks of the optical activities for Te/graphene(L) and Te/graphene(V) heterojunctions are in the MIR range (2500−10 000 nm) and those for the Te/MoS$_2$(L) and Te/MoS$_2$(V) systems are in the NIR + Vis range (380−2500 nm). Second, the highly anisotropic nature of the hybrid systems is manifested in the difference between the in-plane and out-of-plane components of their respective absorbance.

In contrast to the static DFT, Figure 4e−h represents a direct comparison of the time-dependent optical absorbance of all four hybrid systems with respect to those of the pristine ones, computed by using time-dependent density functional theory (TDDFT) formalisms. The details of these calculations are presented in the first section of SI. The outcome of these calculations can be helpful to analyze the time-dependent effects like presence of excitons or interesting light-matter interactions like rotation of the plane of polarization of the incident light. The flat optical responses of graphene, as presented by the blue lines in Figure 4e,f, are modified into broadband distributions, with its peak absorbance in the MIR range (2500−10 000 nm). For MoS$_2$, the TDDFT spectra of both the pristine and hybrid structures are distinctively different in their inherent intricacies from the DFT ones, containing mid-gap states and clear signatures of A and B excitons. For pristine systems, the positions of A and B excitons are at energies 1.31 and 1.33 eV, respectively, as indicated by the blue lines of Figure 4g,h. The exciton positions are energetically underestimated due to the approximations used in the long-range exchange−correlation kernel, as mentioned in Section S2 of SI and also seen in the prior literature.[52] In the TDDFT spectra for the heterojunctions of MoS$_2$, there is a significant shift in the energy positions of the A and B excitons toward higher range by ∼1 eV, as seen in the black plots of Figure 4g,h. The binding energies of the excitons are expressed as the difference in energies of the position of the excitons in the TDDFT-derived absorbance graph with the static optical band gap. Therefore, this huge shift in the energy of the excitons may be related to the enhanced binding energies of both of the excitons. The difference between the VBM and CBM of the decoupled MoS$_2$ in the lateral and vertical heterojunctions, as seen from Figures S7b and S8b, is 1.76 and 1.75 eV, respectively. The difference between these static band edges will be equivalent to the band gap of the decoupled MoS$_2$ in the respective heterojunctions. The differences between these static band gaps with the exciton positions in the TDDFT spectra of Figure 4g,h are equal to the exciton binding energies, as presented in Table 2. When compared with the pristine system, these binding energies indicate a consequential increase in the binding energies of both A and B excitons of MoS$_2$ by ∼200 and 300 meV for lateral and vertical heterojunctions, respectively (Table 2). This increase in the binding energies of the exciton may give rise to an increasing lifetime of the excitons, provided the density of midgap trap states are less within the system.

Henceforth, in addition to the ranges of optical activities of all four heterojunctions encompassing the Vis, NIR, and MIR

Table 2. Excitonic Position of MoS$_2$ before and after the Te-Nanorod Attachment

	A-exciton (eV)	B-exciton (eV)	band gap (eV)	A-exciton BE (eV)	B-exciton BE (eV)
Te/MoS$_2$(L)	2.43	2.47	1.76	0.67	0.71
Te/MoS$_2$(V)	2.31	2.34	1.75	0.56	0.59

range (from 380 to 10 000 nm), these systems also display interesting excitonic effects for MoS$_2$ heterojunctions.

It may also be mentioned in passing that all of these improved functionalities are highly sensitive to the optimized density of Te NRs on top of the 2D ML. With uncontrolled density, the resulting highly hybridized interaction is detrimental to the semiconducting properties, as is evident from Figure S11.

The formation of the hybrid heterojunction also incorporates additional functionalities over the pristine systems. The enhanced DFT + SOC noncollinear spin densities for all of the hybrid heterojunctions and the corresponding spin-projected DOS are plotted in Figures S12−S14, respectively. The interaction of the hybrid systems and their feeble spin polarization with the plane of polarization of the applied illumination also give rise to several optical phenomena like linear dichroism, magneto-optic, and electro-optic Kerr and Faraday effects. The difference between the absorption of the light polarized perpendicular and parallel to the out-of-plane axis can be computed from the linear dichroism. The interaction of the polarized spins of the system with the applied magnetic and electric fields of the incident light results in a rotation of its plane of polarization. These magneto-optical and electro-optical effects are amplified by at least an order of magnitude after the formation of hybrid heterojunctions, as can be seen from Figure S15. The details of these calculations and the results are described in SI.

Therefore, formation of 1D/2D heterojunctions is helpful to remarkably enhance the functionalities of both of the individual components, promoting their application in the field of broadband detection, IR detection, and energy harvesting.

■ CONCLUSIONS

In conclusion, by using first-principles static and time-dependent calculations, we predict an effective design of a 1D/2D hybrid heterojunction by using a single helix of tellurene and the monolayers of 2D materials like graphene and MoS$_2$. The lowest-energy configurations of the four hybrids manifest the type-I, type-II, and Z-scheme heterojunctions, having excellent potential for application in the broadband photodetection, energy harvesting, and longer quasiparticle binding energies. The broad range of optical activities for these heterojunctions encompasses the MIR to NIR and Vis regions and thus predicts an excellent application potential of these systems in the field of photonic IR detectors and green-energy materials.

■ ASSOCIATED CONTENT

ⓢ Supporting Information

The Supporting Information is available free of charge at https://pubs.acs.org/doi/10.1021/acsami.2c13198.

Computational methodology; description of optical property calculations of DFT and TDDFT calculation; decoupled contributions in the band structure of structural distortion and charge redistribution for all four heterojunctions; formation energy of different heterojunctions; description of folding in of high symmetry k-points in graphene; spin-projected magnetic property of heterojunctions; band structure of high-density Te/G and Te/M heterojunction; comparison of Linear dichroism, Kerr effect, and Faraday effect of different heterojunctions; exicition positions of MoS_2 in heterojunction (PDF)

■ AUTHOR INFORMATION

Corresponding Authors

Olle Eriksson − *Department of Physics and Astronomy, Uppsala University, SE-75120 Uppsala, Sweden; School of Science and Technology, Örebro University, SE-70281 Örebro, Sweden*; Email: olle.eriksson@physics.uu.se

Debjani Karmakar − *Department of Physics and Astronomy, Uppsala University, SE-75120 Uppsala, Sweden; Technical Physics Division, Bhabha Atomic Research Centre, Mumbai 400085, India;* ⓘ orcid.org/0000-0002-9619-9493; Email: debjani.karmakar@physics.uu.se

Authors

Tuhin Kumar Maji − *Department of Physics, Indian Institute of Science Bangalore, Bangalore 560012, India*

Kumar Vaibhav − *Computer Division, Bhabha Atomic Research Centre, Mumbai 400085, India*

Anna Delin − *Swedish e-Science Research Center (SeRC), KTH Royal Institute of Technology, SE-10044 Stockholm, Sweden;* ⓘ orcid.org/0000-0001-7788-6127

Complete contact information is available at:
https://pubs.acs.org/10.1021/acsami.2c13198

Notes

The authors declare no competing financial interest.

■ ACKNOWLEDGMENTS

■ REFERENCES

(1) Pradhan, A.; Roy, A.; Tripathi, S.; Som, A.; Sarkar, D.; Mishra, J. K.; Roy, K.; Pradeep, T.; Ravishankar, N.; Ghosh, A. Ultra-high Sensitivity Infra-red Detection and Temperature Effects in a Graphene−tellurium Nanowire Binary Hybrid. *Nanoscale* **2017**, *9*, 9284−9290.

(2) Hou, H.; Zhang, X. Rational Design of 1D/2D Heterostructured Photocatalyst for Energy and Environmental Applications. *Chem. Eng. J.* **2020**, *395*, No. 125030.

(3) Wang, P.; Jia, T.; Wang, B. A Critical Review: 1D/2D Nanostructured Self-supported Electrodes for Electrochemical Water Splitting. *J. Power Sources* **2020**, *474*, No. 228621.

(4) Yang, L.; Lv, Y.; Cao, D. Co,N-codoped Nanotube/Graphene 1D/2D Heterostructure for Efficient Oxygen Reduction and Hydrogen Evolution Reactions. *J. Mater. Chem. A* **2018**, *6*, 3926−3932.

(5) Xiong, J.; Di, J.; Xia, J.; Zhu, W.; Li, H. Surface Defect Engineering in 2D Nanomaterials for Photocatalysis. *Adv. Funct. Mater.* **2018**, *28*, No. 1801983.

(6) Xiao, F.-X.; Miao, J.; Tao, H. B.; Hung, S.-F.; Wang, H.-Y.; Yang, H. B.; Chen, J.; Chen, R.; Liu, B. One-Dimensional Hybrid Nanostructures for Heterogeneous Photocatalysis and Photoelectrocatalysis. *Small* **2015**, *11*, 2115−2131.

(7) Srinivas, V.; Barik, S. K.; Bodo, B.; Karmakar, D.; Chandrasekhar Rao, T. V. Magnetic and Electrical Properties of Oxygen Stabilized Nickel Nanofibers Prepared by the Borohydride Reduction Method. *J. Magn. Magn. Mater.* **2008**, *320*, 788−795.

(8) Luo, B.; Liu, G.; Wang, L. Recent Advances in 2D Materials for Photocatalysis. *Nanoscale* **2016**, *8*, 6904−6920.

(9) Cao, X.; Tian, G.; Chen, Y.; Zhou, J.; Zhou, W.; Tian, C.; Fu, H. Hierarchical Composites of TiO2 Nanowire Arrays on Reduced Graphene Oxide Nanosheets with Enhanced Photocatalytic Hydrogen Evolution Performance. *J. Mater. Chem. A* **2014**, *2*, 4366−4374.

(10) Xia, Y.; Tian, Z.; Heil, T.; Meng, A.; Cheng, B.; Cao, S.; Yu, J.; Antonietti, M. Highly Selective CO2 Capture and Its Direct Photochemical Conversion on Ordered 2D/1D Heterojunctions. *Joule* **2019**, *3*, 2792−2805.

(11) Li, Y.; Wang, L.; Cai, T.; Zhang, S.; Liu, Y.; Song, Y.; Dong, X.; Hu, L. Glucose-assisted Synthesize 1D/2D Nearly Vertical CdS/MoS$_2$ Heterostructures for Efficient Photocatalytic Hydrogen Evolution. *Chem. Eng. J.* **2017**, *321*, 366−374.

(12) Xiao, R.; Zhao, C.; Zou, Z.; Chen, Z.; Tian, L.; Xu, H.; Tang, H.; Liu, Q.; Lin, Z.; Yang, X. In Situ Fabrication of 1D CdS Nanorod/2D Ti3C2 MXene Nanosheet Schottky Heterojunction Toward Enhanced Photocatalytic Hydrogen Evolution. *Appl. Catal., B* **2020**, *268*, No. 118382.

(13) Shang, H.; Chen, H.; Dai, M.; Hu, Y.; Gao, F.; Yang, H.; Xu, B.; Zhang, S.; Tan, B.; Zhang, X.; Hu, P. A Mixed-dimensional 1D Se−2D InSe van der Waals Heterojunction for High Responsivity Self-powered Photodetectors. *Nanoscale Horiz.* **2020**, *5*, 564−572.

(14) Fang, Q.; Shang, Q.; Zhao, L.; Wang, R.; Zhang, Z.; Yang, P.; Sui, X.; Qiu, X.; Liu, X.; Zhang, Q.; Zhang, Y. Ultrafast Charge Transfer in Perovskite Nanowire/2D Transition Metal Dichalcogenide Heterostructures. *J. Phys. Chem. Lett.* **2018**, *9*, 1655−1662.

(15) Jaryal, A.; Battula, V. R.; Kailasam, K. Oxygen Deficient WO3−x Nanorods and g-CN Nanosheets Heterojunctions: A 1D−2D Interface with Engineered Band Structure for Cyclohexanol Oxidation in Visible Light. *ACS Appl. Energy Mater.* **2020**, *3*, 4669−4676.

(16) Gao, Y.; Xu, B. On the Generalized Thermal Conductance Characterizations of Mixed One-Dimensional−Two-Dimensional van der Waals Heterostructures and Their Implication for Pressure Sensors. *ACS Appl. Mater. Interfaces* **2018**, *10*, 14221−14229.

(17) Li, Y.; Huang, L.; Li, B.; Wang, X.; Zhou, Z.; Li, J.; Wei, Z. Co-nucleus 1D/2D Heterostructures with Bi2S3 Nanowire and MoS$_2$ Monolayer: One-Step Growth and Defect-Induced Formation Mechanism. *ACS Nano* **2016**, *10*, 8938−8946.

(18) Sun, G.; Li, B.; Li, J.; Zhang, Z.; Ma, H.; Chen, P.; Zhao, B.; Wu, R.; Dang, W.; Yang, X.; Tang, X.; Dai, C.; Huang, Z.; Liu, Y.; Duan, X.; Duan, X. Direct van der Waals Epitaxial Growth of 1D/2D Sb2Se3/WS2 Mixed-Dimensional *p-n* Heterojunctions. *Nano Res.* **2019**, *12*, 1139−1145.

(19) Wang, K.; Wei, W.; Lou, Z.; Zhang, H.; Wang, L. 1D/2D Heterostructure Nanofiber Flexible Sensing Device with Efficient Gas Detectivity. *Appl. Surf. Sci.* **2019**, *479*, 209−215.

(20) Adekoya, D.; Zhang, S.; Hankel, M. 1D/2D C3N4/Graphene Composite as a Preferred Anode Material for Lithium Ion Batteries: Importance of Heterostructure Design via DFT Computation. *ACS Appl. Mater. Interfaces* **2020**, *12*, 25875−25883.

(21) Mahzoon, S.; Nowee, S. M.; Haghighi, M. Synergetic Combination of 1D-2D g-C$_3$N$_4$ Heterojunction Nanophotocatalyst for Hydrogen Production via Water Splitting under Visible Light Irradiation. *Renewable Energy* 2018, *127*, 433−443.

(22) Liu, Q.; Lu, H.; Shi, Z.; Wu, F.; Guo, J.; Deng, K.; Li, L. 2D ZnIn$_2$S$_4$ Nanosheet/1D TiO$_2$ Nanorod Heterostructure Arrays for Improved Photoelectrochemical Water Splitting. *ACS Appl. Mater. Interfaces* 2014, *6*, 17200−17207.

(23) Xu, B.; He, P.; Liu, H.; Wang, P.; Zhou, G.; Wang, X. A 1D/2D Helical CdS/ZnIn$_2$S$_4$ Nano-Heterostructure. *Angew. Chem., Int. Ed.* 2014, *53*, 2339−2343.

(24) Li, J.-Y.; Li, Y.-H.; Zhang, F.; Tang, Z.-R.; Xu, Y.-J. Visible-light-driven Integrated Organic Synthesis and Hydrogen Evolution Over 1D/2D CdS-Ti$_3$C$_2$Tx MXene Composites. *Appl. Catal., B* 2020, *269*, No. 118783.

(25) Shaari, N.; Kamarudin, S. K.; Zakaria, Z. Potential of Sodium Alginate/titanium Oxide Biomembrane Nanocomposite in DMFC Application. *Int. J. Energy Res.* 2019, *43*, 8057−8069.

(26) Zhang, Z.; Cheng, M.-Q.; Chen, Q.; Wu, H.-Y.; Hu, W.; Peng, P.; Huang, G.-F.; Huang, W.-Q. Monolayer Phosphorene−Carbon Nanotube Heterostructures for Photocatalysis: Analysis by Density Functional Theory. *Nanoscale Res. Lett.* 2019, *14*, No. 233.

(27) Ji, H.; Du, P.; Zhao, D.; Li, S.; Sun, F.; Duin, E. C.; Liu, W. 2D/1D Graphitic Carbon Nitride/titanate Nanotubes Heterostructure for Efficient Photocatalysis of Sulfamethazine Under Solar Light: Catalytic "hot spots" at the Rutile−anatase−titanate Interfaces. *Appl. Catal., B* 2020, *263*, No. 118357.

(28) Xiong, J.; Han, C.; Li, W.; Sun, Q.; Chen, J.; Chou, S.; Li, Z.; Dou, S. Ambient Synthesis of a Multifunctional 1D/2D Hierarchical Ag−Ag$_2$S Nanowire/nanosheet Heterostructure with Diverse Applications. *CrystEngComm* 2016, *18*, 930−937.

(29) Lu, Z.; Liang, D.; Ping, X.; Xing, L.; Wang, Z.; Wu, L.; Lu, P.; Jiao, L. 1D/2D Heterostructures as Ultrathin Catalysts for Hydrogen Evolution Reaction. *Small* 2020, *16*, No. 2004296.

(30) Rogalski, A. Competitive Technologies of Third Generation Infrared Photon Detectors. *Opto-Electron. Rev.* 2006, *14*, 84−98.

(31) Karim, A.; Andersson, J. Y. Infrared detectors: Advances, challenges and new technologies. *IOP Conf. Ser.: Mater. Sci. Eng.* 2013, *51*, No. 012001.

(32) Rogalski, A. HgCdTe Infrared Detector Material: History, Status and Outlook. *Rep. Prog. Phys.* 2005, *68*, 2267−2336.

(33) Zhu, L.; Deng, Z.; Huang, J.; Guo, H.; Chen, L.; Lin, C.; Chen, B. Low Frequency Noise-dark Current Correlations in HgCdTe Infrared Photodetectors. *Opt. Express* 2020, *28*, 23660−23669.

(34) Konstantatos, G.; Howard, I.; Fischer, A.; Hoogland, S.; Clifford, J.; Klem, E.; Levina, L.; Sargent, E. H. Ultrasensitive Solution-cast Quantum Dot Photodetectors. *Nature* 2006, *442*, 180−183.

(35) Ward, M. B.; Karimov, O. Z.; Unitt, D. C.; Yuan, Z. L.; See, P.; Gevaux, D. G.; Shields, A. J.; Atkinson, P.; Ritchie, D. A. On-demand Single-photon Source for 1.3μm Telecom Fiber. *Appl. Phys. Lett.* 2005, *86*, No. 201111.

(36) Rakher, M. T.; Ma, L.; Slattery, O.; Tang, X.; Srinivasan, K. Quantum Transduction of Telecommunications-band Single Photons from a Quantum Dot by Frequency Upconversion. *Nat. Photonics* 2010, *4*, 786−791.

(37) Zhang, K.; Zhang, T.; Cheng, G.; Li, T.; Wang, S.; Wei, W.; Zhou, X.; Yu, W.; Sun, Y.; Wang, P.; Zhang, D.; Zeng, C.; Wang, X.; Hu, W.; Fan, H. J.; Shen, G.; Chen, X.; Duan, X.; Chang, K.; Dai, N. Interlayer Transition and Infrared Photodetection in Atomically Thin Type-II MoTe$_2$/MoS$_2$ van der Waals Heterostructures. *ACS Nano* 2016, *10*, 3852−3858.

(38) Choi, W.; Cho, M. Y.; Konar, A.; Lee, J. H.; Cha, G.-B.; Hong, S. C.; Kim, S.; Kim, J.; Jena, D.; Joo, J.; Kim, S. High-Detectivity Multilayer MoS2 Phototransistors with Spectral Response from Ultraviolet to Infrared. *Adv. Mater.* 2012, *24*, 5832−5836.

(39) Liu, C.-H.; Chang, Y.-C.; Norris, T. B.; Zhong, Z. Graphene Photodetectors with Ultra-broadband and High Responsivity at Room Temperature. *Nat. Nanotechnol.* 2014, *9*, 273−278.

(40) Park, J.; Ahn, Y. H.; Ruiz-Vargas, C. Imaging of Photocurrent Generation and Collection in Single-Layer Graphene. *Nano Lett.* 2009, *9*, 1742−1746.

(41) Xia, F.; Mueller, T.; Golizadeh-Mojarad, R.; Freitag, M.; Lin, Y.-m.; Tsang, J.; Perebeinos, V.; Avouris, P. Photocurrent Imaging and Efficient Photon Detection in a Graphene Transistor. *Nano Lett.* 2009, *9*, 1039−1044.

(42) Mueller, T.; Xia, F.; Avouris, P. Graphene Photodetectors for High-speed Optical Communications. *Nat. Photonics* 2010, *4*, 297−301.

(43) Gabor, N. M.; Song, J. C. W.; Ma, Q.; Nair, N. L.; Taychatanapat, T.; Watanabe, K.; Taniguchi, T.; Levitov, L. S.; Jarillo-Herrero, P. Hot Carrier−Assisted Intrinsic Photoresponse in Graphene. *Science* 2011, *334*, 648−652.

(44) Furchi, M.; Urich, A.; Pospischil, A.; Lilley, G.; Unterrainer, K.; Detz, H.; Klang, P.; Andrews, A. M.; Schrenk, W.; Strasser, G.; Mueller, T. Microcavity-Integrated Graphene Photodetector. *Nano Lett.* 2012, *12*, 2773−2777.

(45) Engel, M.; Steiner, M.; Lombardo, A.; Ferrari, A. C.; Löhneysen, Hv.; Avouris, P.; Krupke, R. Light−matter interaction in a microcavity-controlled graphene transistor. *Nat. Commun.* 2012, *3*, No. 906.

(46) Echtermeyer, T. J.; Britnell, L.; Jasnos, P. K.; Lombardo, A.; Gorbachev, R. V.; Grigorenko, A. N.; Geim, A. K.; Ferrari, A. C.; Novoselov, K. S. Strong Plasmonic Enhancement of Photovoltage in Graphene. *Nat. Commun.* 2011, *2*, No. 458.

(47) Grigorenko, A. N.; Polini, M.; Novoselov, K. S. Graphene Plasmonics. *Nat. Photonics* 2012, *6*, 749−758.

(48) Konstantatos, G.; Badioli, M.; Gaudreau, L.; Osmond, J.; Bernechea, M.; de Arquer, F. P. G.; Gatti, F.; Koppens, F. H. L. Hybrid Graphene−quantum Dot Phototransistors with Ultrahigh Gain. *Nat. Nanotechnol.* 2012, *7*, 363−368.

(49) Britnell, L.; Ribeiro, R. M.; Eckmann, A.; Jalil, R.; Belle, B. D.; Mishchenko, A.; Kim, Y.-J.; Gorbachev, R. V.; Georgiou, T.; Morozov, S. V.; Grigorenko, A. N.; Geim, A. K.; Casiraghi, C.; Neto, A. H. C.; Novoselov, K. S. Strong Light-Matter Interactions in Heterostructures of Atomically Thin Films. *Science* 2013, *340*, 1311−1314.

(50) Maji, T. K.; Vaibhav, K.; Pal, S. K.; Majumdar, K.; Adarsh, K. V.; Karmakar, D. Intricate Modulation of Interlayer Coupling at the Graphene oxide/MoSe$_2$ Interface: Application in Time-dependent Optics and Device Transport. *Phys. Rev. B* 2019, *99*, No. 115309.

(51) Bhatnagar, M.; Gardella, M.; Giordano, M. C.; Chowdhury, D.; Mennucci, C.; Mazzanti, A.; Valle, G. D.; Martella, C.; Tummala, P.; Lamperti, A.; Molle, A.; Buatier de Mongeot, F. Broadband and Tunable Light Harvesting in Nanorippled MoS$_2$ Ultrathin Films. *ACS Appl. Mater. Interfaces* 2021, *13*, 13508−13516.

(52) Rahman, A.; Jennings, J. R.; Tan, A. L.; Khan, M. M. Molybdenum Disulfide-Based Nanomaterials for Visible-Light-Induced Photocatalysis. *ACS Omega* 2022, *7*, 22089−22110.

(53) Zhu, Z.; Cai, C.; Niu, C.; Wang, C.; Sun, Q.; Han, X.; Guo, Z.; Jia, Y.Tellurene-a monolayer of tellurium from first-principles prediction. 2016, arXiv:1605.03253. arXiv.org e-Print archive. https://doi.org/10.48550/arXiv.1605.03253.

(54) Zhu, Z.; Cai, X.; Yi, S.; Chen, J.; Dai, Y.; Niu, C.; Guo, Z.; Xie, M.; Liu, F.; Cho, J.-H.; Jia, Y.; Zhang, Z. Multivalency-Driven Formation of Te-Based Monolayer Materials: A Combined First-Principles and Experimental study. *Phys. Rev. Lett.* 2017, *119*, No. 106101.

(55) Du, Y.; Qiu, G.; Wang, Y.; Si, M.; Xu, X.; Wu, W.; Ye, P. D. One-Dimensional van der Waals Material Tellurium: Raman Spectroscopy under Strain and Magneto-Transport. *Nano Lett.* 2017, *17*, 3965−3973.

(56) Smidstrup, S.; Stradi, D.; Wellendorff, J.; Khomyakov, P. A.; Vej-Hansen, U. G.; Lee, M.-E.; Ghosh, T.; Jónsson, E.; Jónsson, H.; Stokbro, K. First-principles Green's-function Method for Surface Calculations: A Pseudopotential Localized Basis Set Approach. *Phys. Rev. B* 2017, *96*, No. 195309.

(57) Kresse, G.; Hafner, J. Ab initio Molecular Dynamics for Liquid Metals. *Phys. Rev. B* 1993, *47*, 558−561.

(58) Kresse, G.; Hafner, J. Ab initio Molecular-dynamics Simulation of the Liquid-metal–Amorphous-semiconductor Transition in Germanium. *Phys. Rev. B* **1994**, *49*, 14251−14269.

(59) Ernzerhof, M.; Scuseria, G. E. Assessment of the Perdew−Burke−Ernzerhof Exchange-correlation Functional. *J. Chem. Phys.* **1999**, *110*, 5029−5036.

(60) Grimme, S. Semiempirical GGA-type Density Functional Constructed with a Long-Range Dispersion Correction. *J. Comput. Chem.* **2006**, *27*, 1787−1799.

(61) Maji, T. K.; J R, A.; Mukherjee, S.; Alexander, R.; Mondal, A.; Das, S.; Sharma, R. K.; Chakraborty, N. K.; Dasgupta, K.; Sharma, A. M. R.; Hawaldar, R.; Pandey, M.; Naik, A.; Majumdar, K.; Pal, S. K.; Adarsh, K. V.; Ray, S. K.; Karmakar, D. Combinatorial Large-Area MoS_2/Anatase−TiO_2 Interface: A Pathway to Emergent Optical and Optoelectronic Functionalities. *ACS Appl. Mater. Interfaces* **2020**, *12*, 44345−44359.

(62) Manoharan, S.; Krishnamoorthy, K.; Mariappan, V. K.; Kesavan, D.; Kim, S.-J. Electrochemical deposition of vertically aligned tellurium nanorods on flexible carbon cloth for wearable supercapacitors. *Chem. Eng. J.* **2021**, *421*, No. 129548.

(63) Yuan, J.; Schmalz, H.; Xu, Y.; Miyajima, N.; Drechsler, M.; Möller, M. W.; Schacher, F.; Müller, A. H. E. Room-Temperature Growth of Uniform Tellurium Nanorods and the Assembly of Tellurium or Fe_3O_4 Nanoparticles on the Nanorods. *Adv. Mater.* **2008**, *20*, 947−952.

(64) Guan, Z.; Ni, S.; Hu, S. Band gap opening of graphene by forming a graphene/$PtSe_2$ van der Waals heterojunction. *RSC Adv.* **2017**, *7*, 45393−45399.

(65) García-Lastra, J. M. Strong dependence of band-gap opening at the Dirac point of graphene upon hydrogen adsorption periodicity. *Phys. Rev. B* **2010**, *82*, No. 235418.

(66) Maji, T. K.; Sarkar, P. K.; Kar, P.; Liu, B.; Lemmens, P.; Karmakar, D.; Pal, S. K. A Combined Experimental and Computational Study on a Nanohybrid Material for Potential Application in NIR Photocatalysis. *Appl. Catal., A* **2019**, *583*, No. 117124.

(67) Gadde, J. R.; Karmakar, A.; Maji, T. K.; Mukherjee, S.; Alexander, R.; Sharma, A. M. R.; Das, S.; Mandal, A.; Dasgupta, K.; Naik, A.; Majumdar, K.; Hawaldar, R.; Adarsh, K. V.; Ray, S. K.; Karmakar, D. Two-dimensional ReS_2: Solution to the Unresolved Queries on Its Structure and Inter-layer Coupling Leading to Potential Optical Applications. *Phys. Rev. Mater.* **2021**, *5*, No. 054006.

(68) Karmakar, D.; Halder, R.; Padma, N.; Abraham, G.; Vaibhav, K.; Ghosh, M.; Kaur, M.; Bhattacharya, D.; Rao, T. V. C. Optimal Electron Irradiation as a Tool for Functionalization of MoS_2: Theoretical and Experimental Investigation. *J. Appl. Phys.* **2015**, *117*, No. 135701.